

Voltage control of ferrimagnetic order and voltage-assisted writing of ferrimagnetic spin textures

Mantao Huang, Muhammad Usama Hasan, Konstantin Klyukin, Delin Zhang, Deyuan Lyu, Pierluigi Gargiani, Manuel Valvidares, Sara Sheffels, Alexandra Churikova, Felix Büttner, Jonas Zehner, Lucas Caretta, Ki-Young Lee, Joonyeon Chang, Jian-Ping Wang, Karin Leistner, Bilge Yildiz, Geoffrey S. D. Beach

Angaben zur Veröffentlichung / Publication details:

Huang, Mantao, Muhammad Usama Hasan, Konstantin Klyukin, Delin Zhang, Deyuan Lyu, Pierluigi Gargiani, Manuel Valvidares, et al. 2021. "Voltage control of ferrimagnetic order and voltage-assisted writing of ferrimagnetic spin textures." *Nature Nanotechnology* 16 (9): 981-88.
<https://doi.org/10.1038/s41565-021-00940-1>.

Nutzungsbedingungen / Terms of use:

licgercopyright

Dieses Dokument wird unter folgenden Bedingungen zur Verfügung gestellt: / This document is made available under the following conditions:

Deutsches Urheberrecht

Weitere Informationen finden Sie unter: / For more information see:

<https://www.uni-augsburg.de/de/organisation/bibliothek/publizieren-zitieren-archivieren/publizieren>



Voltage control of ferrimagnetic order and voltage-assisted writing of ferrimagnetic spin textures

Mantao Huang¹, Muhammad Usama Hasan¹, Konstantin Klyukin¹, Delin Zhang², Deyuan Lyu², Pierluigi Gargiani³, Manuel Valvidares³, Sara Sheffels¹, Alexandra Churikova¹, Felix Büttner¹, Jonas Zehner^{4,5}, Lucas Caretta¹, Ki-Young Lee⁶, Joonyeon Chang^{6,7}, Jian-Ping Wang², Karin Leistner^{4,5}, Bilge Yildiz^{1,8} and Geoffrey S. D. Beach¹✉

Voltage control of magnetic order is desirable for spintronic device applications, but 180° magnetization switching is not straightforward because electric fields do not break time-reversal symmetry. Ferrimagnets are promising candidates for 180° switching owing to a multi-sublattice configuration with opposing magnetic moments of different magnitudes. In this study we used solid-state hydrogen gating to control the ferrimagnetic order in rare earth-transition metal thin films dynamically. Electric field-induced hydrogen loading/unloading in GdCo can shift the magnetic compensation temperature by more than 100 K, which enables control of the dominant magnetic sublattice. X-ray magnetic circular dichroism measurements and ab initio calculations indicate that the magnetization control originates from the weakening of antiferromagnetic exchange coupling that reduces the magnetization of Gd more than that of Co upon hydrogenation. We observed reversible, gate voltage-induced net magnetization switching and full 180° Néel vector reversal in the absence of external magnetic fields. Furthermore, we generated ferrimagnetic spin textures, such as chiral domain walls and skyrmions, in racetrack devices through hydrogen gating. With gating times as short as 50 μs and endurance of more than 10,000 cycles, our method provides a powerful means to tune ferrimagnetic spin textures and dynamics, with broad applicability in the rapidly emerging field of ferrimagnetic spintronics.

Controlling the magnetic state of devices by electrical means is critical for spin-based data storage and logic^{1,2}. One of the key technological challenges is to achieve efficient 180° magnetic switching by electrical means. Current methods are mostly based on local magnetic fields or spin torques^{3,4}. Due to a much lower energy consumption^{5,6}, voltage-controlled magnetization switching is desirable. However, it is inherently difficult because electric fields do not induce the required time-reversal symmetry breaking for 180° magnetic switching. Many methods, such as using piezoelectric and multiferroic materials^{5,7–11}, are being explored for voltage-controlled magnetization switching. However, these methods involve either high voltages for inducing enough strain, or difficult fabrication procedures.

Multi-sublattice materials present unique opportunities for voltage control of magnetism^{12,13}, with ferrimagnets being promising for achieving 180° switching owing to their multi-sublattice configuration with magnetic moments of different magnitudes opposing each other. By tuning the relative sublattice magnetization magnitudes, the net magnetization can be reversed. Moreover, compared with ferromagnets, ferrimagnets offer technological advantages as they allow for small spin textures¹⁴, fast spin dynamics^{14–16} and ultrafast optical switching¹⁷. However, the conventional approaches to controlling the compensation of ferrimagnets, such as varying the composition at fabrication¹⁸, annealing^{19,20}, heating or cooling²¹ and

hydrogen gas exposure^{22,23}, do not allow for localized electrical actuation. Ultrashort light pulses have been shown to enable all-optical switching of ferrimagnets^{17,24,25}, however, the need for an ultrafast laser source may complicate device designs and the optical paths may be difficult to scale.

Here, we show the reversible control of the dominant sublattice of a rare earth-transition metal (RE-TM) alloy ferrimagnet (GdCo) by a gate voltage (V_G) using a solid-state hydrogen pump²⁶. The control originates from the injection of hydrogen, sourced from ambient moisture through hydrolysis, into GdCo, which tunes the relative sublattice magnetizations and hence the degree of compensation. By applying a small V_G , the compensation temperature (T_M) can be shifted by >100 K, and the dominant sublattice can be reversibly switched under ambient, isothermal conditions. Element-specific X-ray magnetic circular dichroism (XMCD) revealed that hydrogenation reduces the sublattice magnetization of Gd substantially, but only modestly reduces that of Co. Mean-field modelling of the experimental data combined with ab initio calculations suggest that this results from hydrogen-induced reduction of the inter-sublattice exchange coupling strength that is largely responsible for the Gd sublattice order. We demonstrate here that the dominant sublattice can be toggled using pulses as short as 50 μs at room temperature, and that the devices show no degradation after >10⁴ gating cycles. Using appropriately designed

¹Department of Materials Science and Engineering, Massachusetts Institute of Technology, Cambridge, MA, USA. ²Department of Electrical and Computer Engineering, University of Minnesota, Minneapolis, MN, USA. ³ALBA Synchrotron Light Source, Barcelona, Spain. ⁴Faculty of Natural Sciences, Institute of Chemistry, Electrochemical Sensing and Energy Storage, Chemnitz University of Technology, Chemnitz, Germany. ⁵Leibniz IFW Dresden, Dresden, Germany. ⁶Center for Spintronics, Korea Institute of Science and Technology, Seoul, Korea. ⁷Yonsei-KIST Convergence Research Institute, Yonsei University, Seoul, Korea. ⁸Department of Nuclear Science and Engineering, Massachusetts Institute of Technology, Cambridge, MA, USA. ✉e-mail: gbeach@mit.edu

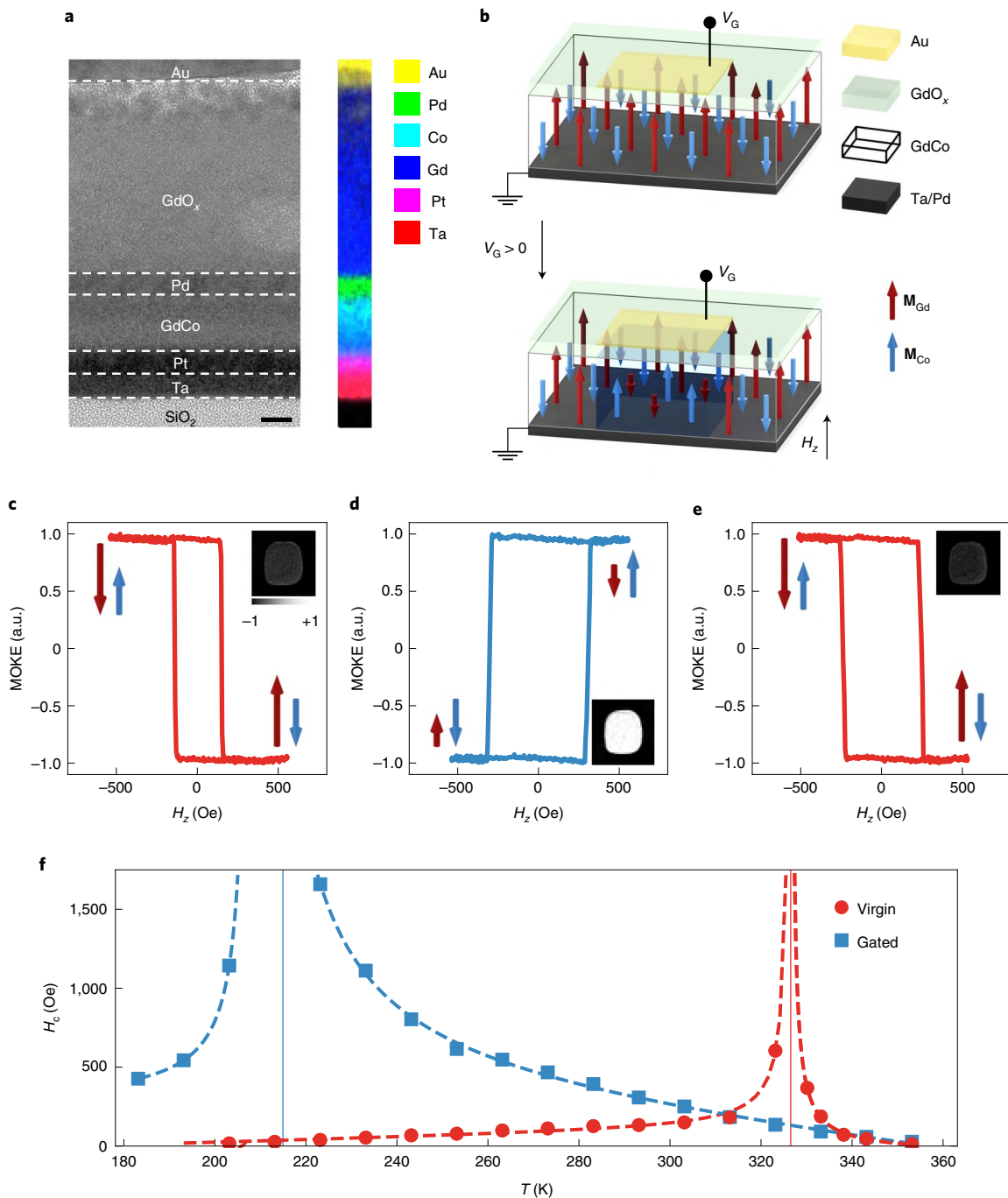


Fig. 1 | Dominant sublattice toggling and compensation temperature gating of GdCo. **a**, Cross-sectional high-resolution transmission electron micrograph (left) and energy-dispersive X-ray spectroscopic chemical profile (right) of a GdCo heterostructure. Scale bar, 5 nm. **b**, Schematic illustration of the device in the virgin state (top) and after applying a positive gate voltage (bottom). The Pd protection layer on top of the GdCo layer has been omitted. The arrows represent the ferrimagnetic alignment of sublattice magnetization (M_{Gd} and M_{Co}). **c–e**, Laser MOKE hysteresis loops measured at the gate region of the device as fabricated (**c**), after applying $V_G = +2.5$ V for 180 s (**d**) and after applying $V_G = -0.5$ V subsequently for 30 s. Insets: differential wide-field MOKE images of the gate area. The colour bar for the MOKE contrast images is shown in the inset to **c**. The values -1 and $+1$ (a.u.) indicate that the Co sublattice aligns antiparallel and parallel to the external field, respectively. All three images share the same colour scale. **f**, Coercivity (H_c) versus temperature in the virgin state (red circles) and after applying a positive V_G (blue squares), showing hydrogen gating induces a decrease in T_M of >100 K. The dashed lines are for guidance only. The red and blue vertical lines indicate the estimated compensation temperatures for virgin and gated states, respectively. Adapted with permission from ref. ⁵⁰, MIT.

heterostructures, we have achieved external-field-free deterministic 180° reversal of either the net magnetization or the Néel vector using a gate voltage alone, showing that this strategy has promise for device implementation. Finally, reversed domain and skyrmion

bubble can be generated in racetrack devices because the approach allows for localized electrical control. This approach provides a new platform for voltage control of magnetism and enables a new type of magnetic bit writing.

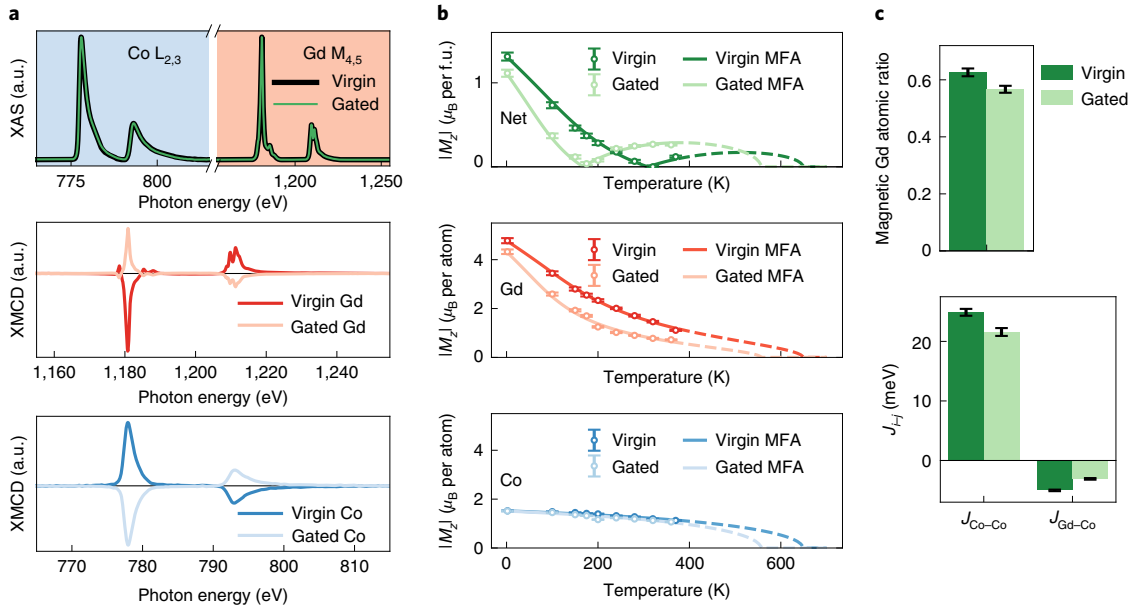


Fig. 2 | XMCD and MFA modelling of the effect of hydrogen gating on GdCo. **a**, Exemplary Co L_{2,3} and Gd M_{4,5} XAS spectra (top) and XMCD spectra (middle and bottom) before and after application of a positive V_G at $T = 280$ K. The virgin XAS spectra are drawn with thicker black lines while the gated XAS spectra are drawn in thinner green lines. **b**, Net magnetization (top) and magnetization of Gd and Co (middle and bottom) as a function of temperature before and after application of a positive V_G . The error bars represent propagated errors from the variations in the XMCD integral of the Gd M₅ peak or the Co L₃ peak (p) and the total XMCD integral (q) from the choice of integration limits of the sum rule. The solid lines show the results of MFA modelling, and the dashed lines show extrapolated modelling results. f.u., formula unit Gd_{0.45}Co_{0.55}. **c**, Extracted model parameters from MFA modelling showing the ratio of Gd atoms that are magnetic (top) and exchange coupling strengths (bottom). The error bars represent standard deviation errors of the parameters.

Dominant sublattice switching and T_M gating

Our experiments focused on amorphous Gd_xCo_{100-x} (GdCo), an perpendicularly magnetized ferrimagnet with antiparallel Gd and Co sublattices. Because the magnitude ($|\mathbf{M}_{\text{Gd}}|$) of the Gd sublattice magnetization (\mathbf{M}_{Gd}) varies more strongly with T than does the magnitude ($|\mathbf{M}_{\text{Co}}|$) of the Co sublattice magnetization (\mathbf{M}_{Co})²⁷, the dominant sublattice depends on the alloy composition and temperature (T). We studied voltage-controlled hydrogen gating in Ta/(Pd or Pt)/Gd₄₅Co₅₅/Pd/GdO_x/Au films grown on thermally oxidized Si (see Methods). The amorphous nature of the GdCo layer is confirmed by the cross-sectional transmission electron micrograph in Fig. 1a. The composition of the GdCo layer was chosen such that the net magnetization ($\mathbf{M} = \mathbf{M}_{\text{Gd}} + \mathbf{M}_{\text{Co}}$) is Gd-dominant ($|\mathbf{M}_{\text{Gd}}| > |\mathbf{M}_{\text{Co}}|$) at room temperature (Supplementary Information). Under positive V_G , the top GdO_x/Au gate catalyses water dissociation sourced from ambient humidity and proton injection (ref. 26). The upper Pd layer protects the GdCo from oxidation and allows hydrogen to diffuse through²⁸.

To study the effect of V_G on the ferrimagnetic order, the top Au layer was patterned into isolated electrodes on an otherwise continuous film. The bottom metal layers (Ta/Pd) serve as the back electrode, allowing for localized gating (Fig. 1b; see Methods). The polar magneto-optical Kerr effect (MOKE) was used to measure the out-of-plane hysteresis loops with a focused laser spot positioned over the gate. It has been shown^{26,29,30} that in metal/GdO_x/Au stacks, the application of a positive gate voltage $V_G \gtrsim 1.2$ V leads to the dissociation of water molecules at the Au/GdO_x interface and injects protons toward the bottom electrode where they form neutral H by recombining with electrons. A negative V_G reverses the process, allowing for solid-state hydrogen loading/unloading. Figure 1c–e shows the GdCo hysteresis loops measured in the virgin state (Fig. 1c), after applying $V_G = +2.5$ V (180 s) (Fig. 1d) and after subsequently applying $V_G = -0.5$ V (30 s) (Fig. 1e). The data show a

reversible voltage-gated inversion of the MOKE polarity, which is localized in the gate region as seen in wide-field differential MOKE contrast images (insets in Fig. 1c–e; see Methods). The Kerr rotation in GdCo arises primarily from the Co sublattice³¹. Therefore, this inversion suggests that \mathbf{M}_{Co} switches from being antiparallel (determined by the initial composition of GdCo) to parallel with respect to \mathbf{M} under positive V_G ; that is, the dominant sublattice switches from Gd to Co (Fig. 1b) upon hydrogen loading.

Figure 1f shows the coercivity (H_c) versus T before and after applying $V_G = +2.5$ V. The divergence of H_c occurs at the magnetization compensation temperature (T_M), at which $|\mathbf{M}_{\text{Co}}| = |\mathbf{M}_{\text{Gd}}|$ and hence $|\mathbf{M}| = 0$. The virgin state has a $T_M \approx 330$ K, consistent with a Gd-dominant \mathbf{M} at room temperature. After gating, T_M decreases to ~ 220 K, so the room-temperature magnetization is Co-dominant, consistent with the inversion of MOKE polarity observed in Fig. 1d. Gating experiments conducted under different atmospheric conditions (Supplementary Information) confirmed that this effect only occurs when water is present in the gas environment, consistent with hydrogen gating by water hydrolysis at the top electrode²⁶. This remarkable change in T_M , by >100 K, shows that hydrogen gating allows for facile solid-state control of ferrimagnetic order and 180° switching of \mathbf{M} by tuning the relative magnitude of \mathbf{M}_{Gd} and \mathbf{M}_{Co} using a small V_G .

Hydrogen-enabled switching of ferrimagnetic order

To gain mechanistic insight into the observed T_M gating by hydrogenation, we used element-specific XMCD in transmission to directly measure the thickness-averaged Gd and Co sublattice magnetizations and their change upon V_G application. The geometry and auxiliary layers of the devices discussed above were modified for XMCD measurement (see Methods) while the GdCo layer was kept the same. Figure 2a shows exemplary X-ray absorption spectroscopy (XAS) and XMCD spectra of the Gd M_{4,5} and Co L_{2,3} edges

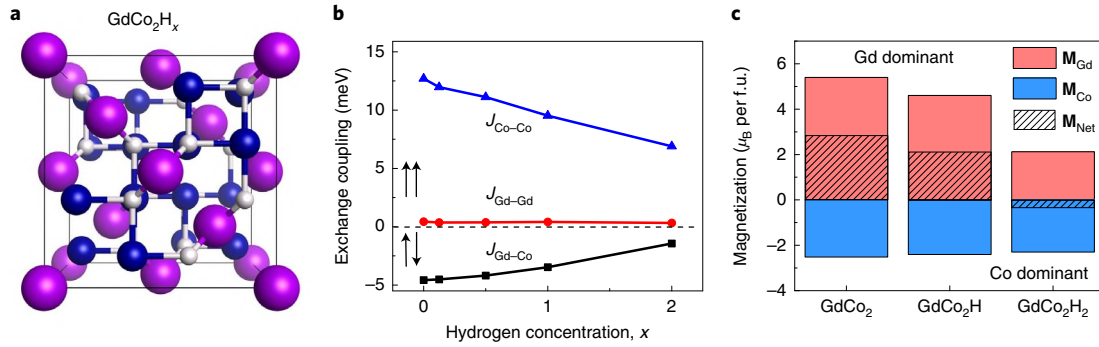


Fig. 3 | Ab initio calculations of the effect of hydrogen loading. **a**, Crystal structure of the model system GdCo₂H_x (C15 Laves phase). The purple, blue and small white spheres represent Gd, Co and H atoms, respectively. **b**, Exchange coupling constants (J_{ij}) versus hydrogen loading in GdCo₂H_x, obtained by DFT calculations. **c**, Sublattice and net magnetizations of GdCo₂H_x at $T = 300$ K obtained from spin dynamics modelling. Adapted with permission from ref. ⁵⁰, MIT.

at 280 K before and after applying $V_G = +5$ V for 5 min, measured with a fixed out-of-plane field of 1 T. The XAS spectra are indistinguishable before and after gating, however, the signs of both the Gd and Co XMCD signals invert, indicating the dominant sublattice switched from Gd to Co, consistent with Fig. 1f.

The temperature dependence of the sublattice magnetization was extracted from similarly collected XMCD spectra before and after gating using the dichroism sum rules (Fig. 2b; see Methods). The magnetization of Gd exhibits a sizable reduction upon gating, whereas that of Co changes much less. To further understand the fundamental mechanism of the observed changes, we modelled the temperature dependence using a two-sublattice mean-field approximation (MFA; see Methods). The modelling results (Fig. 2b) agree well with the experimental data. The extracted model parameters (Fig. 2c) suggest that hydrogen loading induces a much larger fractional decrease in the inter-sublattice exchange coupling strength ($J_{\text{Gd-Co}}$) than the Co intra-sublattice exchange coupling strength ($J_{\text{Co-Co}}$). The decrease in $J_{\text{Gd-Co}}$ reduces the finite-temperature M_{Gd} , which we identify as the origin of the observed dominant sublattice toggling and T_M gating.

To further understand the mechanism, we performed density functional theory (DFT) calculations with a crystalline GdCo₂ supercell model system (Fig. 3a). Ab initio calculations revealed that the zero-temperature Gd moment is insensitive to hydrogenation as the f electrons are highly localized, and the Co moment varies only slightly upon hydrogenation (Supplementary Information). This alone is insufficient to explain the dominant sublattice switching. We further studied the effect of hydrogenation on inter- and intra-lattice exchange interactions using a Heisenberg model (see Methods). The results show that $J_{\text{Gd-Co}}$ decreases drastically upon hydrogenation, whereas $J_{\text{Co-Co}}$ experiences a more modest fractional decrease (Fig. 3b). Because Gd–Gd exchange coupling is weak, $J_{\text{Gd-Co}}$ is predominantly responsible for stabilizing $|M_{\text{Gd}}|$ at finite temperature. Monte-Carlo spin dynamics simulations (see Methods) for GdCo₂, GdCo₂H and GdCo₂H₂ (Fig. 3c) using the DFT-calculated exchange constants show that although GdCo₂ is dominated by Gd at room temperature^{32,33}, the net magnetization is reduced in GdCo₂H due to a reduction in $|M_{\text{Gd}}|$ relative to $|M_{\text{Co}}|$, and the dominant sublattice is reversed for GdCo₂H₂. These results qualitatively agree with the XMCD results and point to hydrogen-gated modulation of $J_{\text{Gd-Co}}$ as the origin of the experimentally observed shift in T_M . Although ab initio calculations were performed for crystalline unit cells for computational efficiency, the qualitative behaviour is expected to be similar for the amorphous GdCo in the experiments because second-nearest-neighbour exchange constants are negligible (Supplementary Information).

Reversibility and speed of dominant sublattice gating

We next examined the reversibility of sublattice switching electrically using devices with a standard Hall cross geometry (see Methods and Fig. 4a). Out-of-plane hysteresis loops were measured by means of the anomalous Hall effect (AHE) resistance (R_{AHE}) while applying V_G . Similarly to MOKE contrast, R_{AHE} arises primarily from Co^{18,34–36}, because the rare-earth 4f electrons are far below the Fermi level, so the AHE probes the orientation of M_{Co} in the coupled system. Therefore, similarly to MOKE contrast, the toggling of the dominant sublattice by V_G should manifest as an inversion of the AHE hysteresis loop. Figure 4b shows the time sequence of H_c acquired as V_G was cycled between +3 and –1.5 V (see also Supplementary Video for the hysteresis loops). Starting in the Gd-dominant state, the positive V_G causes H_c to first increase rapidly, as the GdCo is driven through compensation, and then to decrease after the inversion of the AHE loop. The negative V_G brings the GdCo back through compensation to the Gd-dominant state. Because the change is continuous, the degree of compensation can be precisely tuned by controlling the V_G and dwell time, providing analogue access to intermediate states with a wide range of H_c in both polarities.

The time required to toggle the dominant sublattice at room temperature can be substantially shortened by using a V_G of larger amplitude. The hysteresis loop of a device starting in the Gd-dominant state inverted after applying a pulse of +16 V for 50 μs (Fig. 4c). This is more rapid than other recent reports of magneto-ionic switching (for example ref. ²⁶). Even faster switching should be accessible with a higher V_G or a thinner GdO_x layer to achieve a higher electric field.

Figure 4d shows the AHE loop polarity versus cycle number as the device was cycled >10,000 times between the Gd- and Co-dominant states (see Methods), and also the hysteresis loops at Cycles 1 and 10,000. The results show that the magnetic property switching is remarkably reversible, with no evidence of device wear out or irreversible changes of the magnetic property after an unprecedented degree of cycling.

Field-free net magnetization and Néel vector reversal

The net magnetization vector $\mathbf{M} = \mathbf{M}_{\text{Co}} + \mathbf{M}_{\text{Gd}}$ and the Néel vector $\mathbf{N} = \mathbf{M}_{\text{Co}} - \mathbf{M}_{\text{Gd}}$ are parallel (antiparallel) to one another in the Co (Gd)-dominant states. Therefore, fixing the direction of \mathbf{M} can allow the direction of \mathbf{N} to be inverted by V_G , and vice versa. Here, we demonstrate deterministic, 180° voltage-controlled reversal of either \mathbf{M} or \mathbf{N} in the absence of an external magnetic field using appropriate biasing layers.

The direction of \mathbf{M} naturally inverts as GdCo is driven across the compensation point; to make this process deterministic, that is, to ensure that a given voltage polarity leads to a well-defined

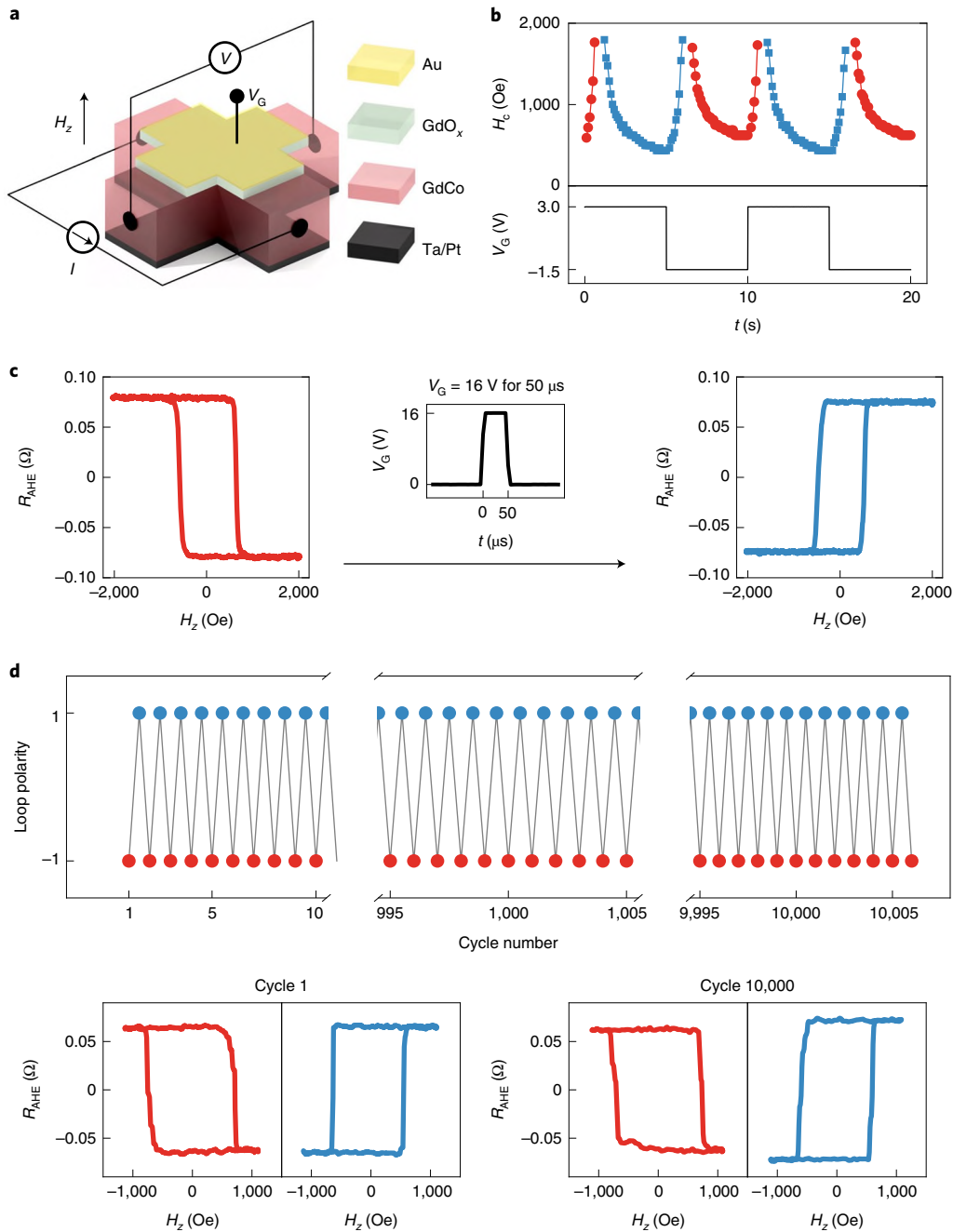


Fig. 4 | Reversibility and speed of dominant sublattice gating characterized by electrical measurements. **a**, Schematic illustration of the Hall cross device structure. The Pd protection layer on top of the GdCo layer has been omitted. I , current; V , voltage. **b**, Coercivity (H_c) of hysteresis loops versus time, acquired as V_G was cycled between +3 V (5 s) and -1.5 V (5 s), starting in the Gd-dominant state. The red circles and blue squares indicate the Gd-dominant and Co-dominant states, respectively. **c**, AHE hysteresis loops measured before (left) and after (right) the application of a V_G pulse (+16 V, 50 μ s). The waveform of the V_G pulse is shown in the middle. **d**, AHE hysteresis loop polarity as a function of cycle number, showing >10,000 reversible cycles (top). AHE hysteresis loops of a device at the 1st and 10,000th cycle, in the Gd-dominant (red) and Co-dominant (blue) states (bottom). No irreversible changes in the hysteresis loop are observed. Adapted with permission from ref. ⁵⁰, MIT.

direction of \mathbf{M} , we integrated an exchange-biasing NiO anti-ferromagnet underlayer to pin the sublattice orientations of a Gd-dominant GdCo film (Fig. 5a; see Methods). The exchange bias direction was set by a fixed magnetic field during growth. The fully shifted hysteresis loop (Fig. 5b) implies that the zero-field orientation of \mathbf{M} , and hence of \mathbf{M}_{Gd} , lies along the positive field direction. Application of a positive V_G leads to a MOKE polarity inversion, corresponding to changing from a Gd-dominant to a Co-dominant state, but the sign of the MOKE signal at remanence,

which tracks the orientation of \mathbf{M}_{Co} , is unchanged. Because the sublattice orientations at remanence are the same, the direction of \mathbf{M} inverts upon hydrogen loading/unloading, which accounts for the observed change in sign of the exchange bias field. This functionality, namely voltage control of the net magnetization, would be desirable in a variety of potential applications, such as dipole-coupled nanomagnetic logic^{37,38}, reconfigurable magnonic crystals based on magnetostatic spin waves^{39,40} and stray field control and steering of fluid-borne particles^{41,42}.

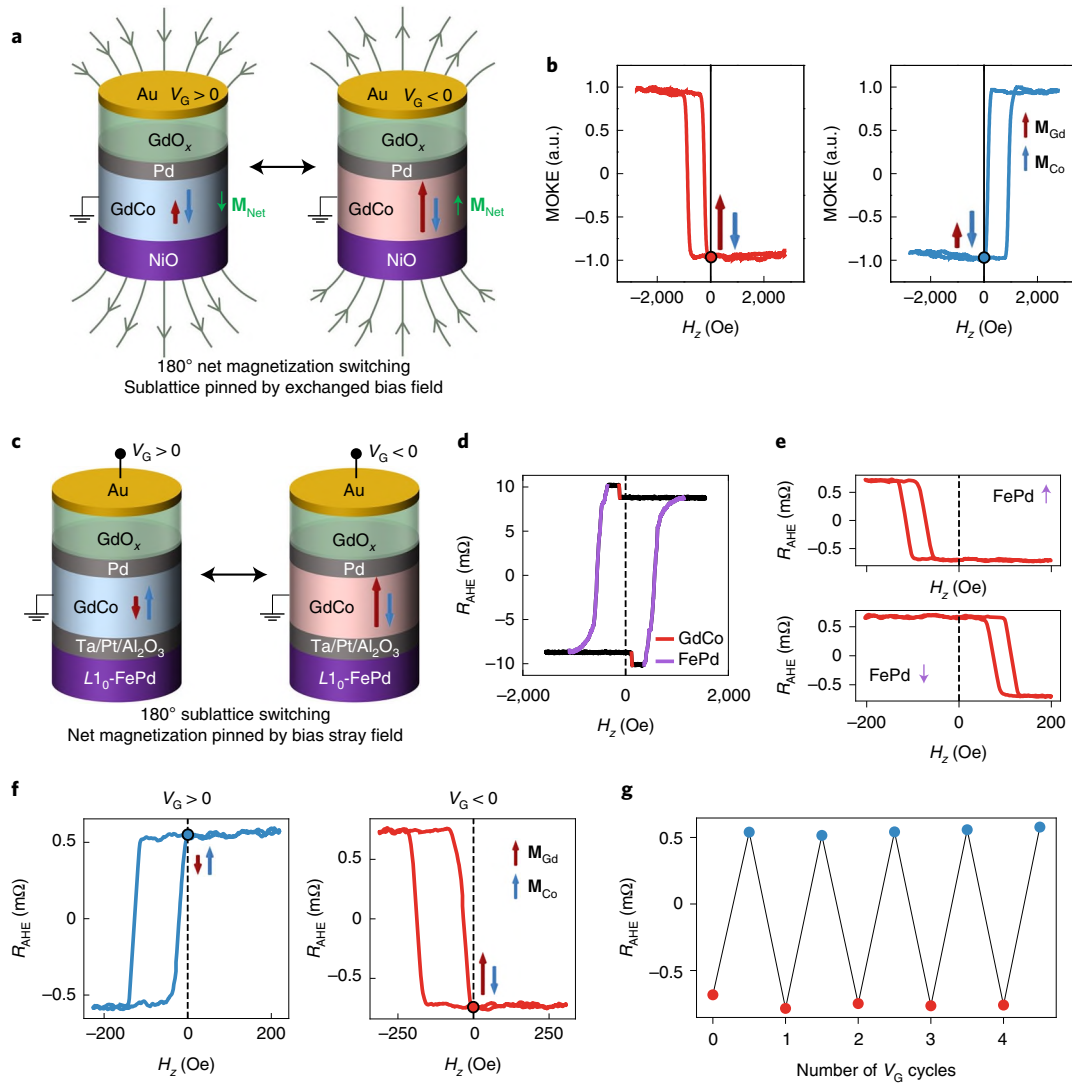


Fig. 5 | Deterministic 180° voltage-controlled reversal of net magnetization and Néel vector in the absence of an external field. **a**, Schematic illustration of the device layer structure demonstrating deterministic 180° voltage-controlled reversal of net magnetization when loaded (left) and unloaded (right) with hydrogen. The Pd layer between NiO and GdCo is omitted. **b**, MOKE hysteresis loops as-fabricated (left) and after applying $V_G = +1.8$ V for 240 s (right) with hydrogen. The sublattice magnetization orientations are fixed in the absence of an external field and the net magnetization orientation is switched 180°. **c**, Schematic illustration of the device layer structure demonstrating external-field-free switching of the Néel vector when loaded (left) and unloaded (right) with hydrogen. An $L1_0$ -FePd nanomagnet at the bottom provides stray field to pin the orientation of the net magnetization. The layers below the $L1_0$ -FePd layer are omitted. **d**, AHE hysteresis loop of the device with both GdCo and FePd. **e**, Minor AHE hysteresis loops showing the bias field from the FePd layer when it is saturated up (top) and down (bottom). **f**, With the FePd magnetization saturated upwards, the minor hysteresis loops of the device when loaded (left) and unloaded (right) with hydrogen upon application of $V_G = +2.5$ and -1.6 V, respectively. **g**, R_{AHE} measured when V_G was cycled between $+2.5$ and -1.6 V, showing reversible switching of the sublattices.

By replacing the NiO layer with a stray field biasing layer, the preferred direction of \mathbf{M} can instead be fixed, allowing for controlling the orientation of \mathbf{N} . We achieved this by integrating an $L1_0$ -FePd layer with bulk perpendicular magnetic anisotropy^{43,44} as a stray field pinning layer (Fig. 5c). The major hysteresis loop shown in Fig. 5d, measured in a Hall cross device using the AHE, shows that the H_c of the FePd layer (~ 560 Oe) is much higher than that of the GdCo layer (~ 20 Oe). The minor hysteresis loops (Fig. 5e), acquired after saturating the FePd in either the ‘up’ or ‘down’ orientation, show that the stray field fully shifts the GdCo hysteresis loop, leading to a fixed, deterministic orientation of \mathbf{M} at zero external field. Figure 5f,g show that hydrogen loading/unloading toggles the zero-field sign of the AHE (Supplementary Information), which, because it tracks the orientation of \mathbf{M}_{Co} , indicates that the sublattice orientations, and hence \mathbf{N} , can be repeatedly reversed by gate

voltage cycling. We note that in this case a magnetic field is required to break the time-inversion symmetry, however, the field direction is fixed and its source can be integrated into the device, similarly to spin-orbit torque (SOT) switching devices^{45,46}, which also require a fixed bias field for operation.

Reversed domain and skyrmion generation

The localized nature of the hydrogen gating allows for applications such as reversed domain and skyrmion generators in racetrack devices, as demonstrated in Fig. 6. The reversed domain generator consists of a patterned domain wall track and a rectangular gate (Fig. 6a; see Methods). The asymmetric heavy-metal layers above and below GdCo give rise to a Dzyaloshinskii–Moriya interaction and current-induced spin-orbit torque^{14,47}, stabilizing Néel domain walls that can be readily displaced by current. The device was

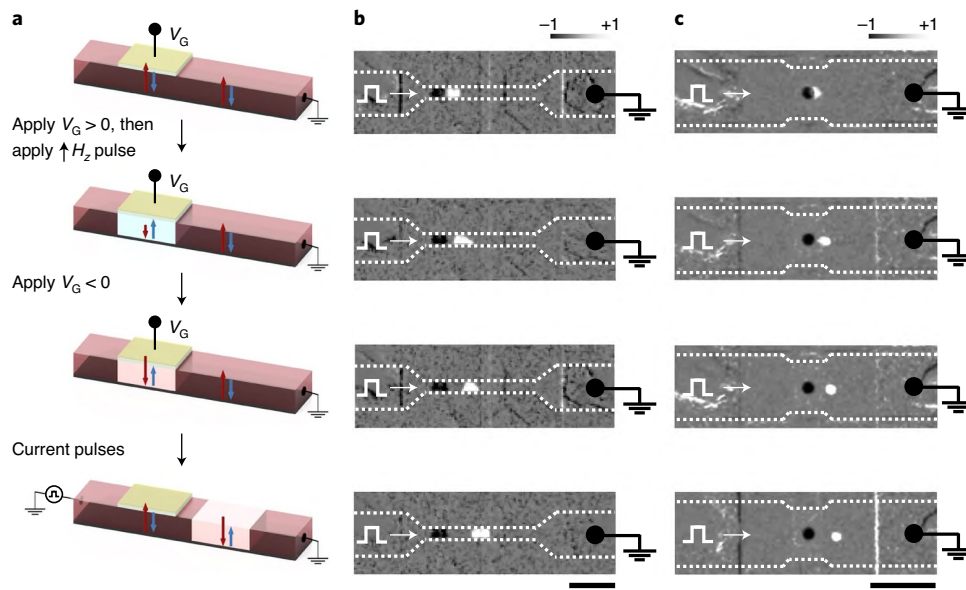


Fig. 6 | Reversed domain and skyrmion generation based on voltage gating of GdCo. **a**, Schematic illustration of the device structure and operation procedure of the reversed domain generator. The Pd protection layer on top of the GdCo layer has been omitted. **b**, Wide-field MOKE contrast images. **c**, Current-driven movement of the generated bubble skyrmion, captured by a sequence of wide-field MOKE contrast images. The colour bars for the differential wide-field MOKE contrast are shown top right in **b** and **c**. The values -1 and $+1$ (a.u.) indicate that the Co sublattice orientation changes from up to down and from down to up, respectively. Scale bars, $100\ \mu\text{m}$. Adapted with permission from ref. ⁵⁰, MIT.

initialized with a positive out-of-plane magnetic field pulse. In order to generate a reversed domain in the gate region (Fig. 6a), a positive V_G was applied to switch the gated region from Gd-dominant to Co-dominant. Then a positive out-of-plane magnetic field pulse was applied to set the direction of \mathbf{M} to point up and locally switch \mathbf{N} under the gate, after which a negative V_G restored the gated region to a Gd-dominant state. Figure 6b shows a sequence of differential MOKE contrast images as the generated reversed ferrimagnetic domain was moved along the track by longitudinal current pulses. Both up–down and down–up domain walls moved towards the current flow direction, consistent with SOT-driven left-handed Néel domain wall movements⁴⁸. After the reversed domain was moved out of the gate region, the gate region shows dark contrast as \mathbf{M}_{Co} switched from up to down, and the reversed domain exhibits brighter contrast as \mathbf{M}_{Co} switched from down to up. This result shows that V_G in conjunction with a global out-of-plane external magnetic field pulse enables the writing of a reversed domain in a defined region, which can subsequently be displaced by current along a racetrack. As demonstrated in Fig. 5c–g, the external out-of-plane field can potentially be replaced by a localized pinned stray field layer.

To further demonstrate the versatility of this approach, we fabricated skyrmion generators with a similar structure to the reversed domain generator, except for the addition of an Al_2O_3 hydrogen blocking layer between the GdO_x and Pd layers (see Methods). To confine the hydrogen loading, we patterned the Al_2O_3 layer with a circular hole beneath the rectangular gate. Following the same procedure as for the generation of a reversed domain, a circular reversed domain in the middle of a racetrack was nucleated and then moved by current (Fig. 6c). The motion direction of the domain indicates that it is a left-handed Néel bubble skyrmion. It can be shifted bidirectionally by reversing the current polarity (Supplementary Information).

Conclusions

We have demonstrated here the reversible control of the dominant sublattice of a ferrimagnet by a gate voltage in an all-solid-state structure. The control originates from the injection of hydrogen,

sourced from the hydrolysis of H_2O in ambient moisture, into GdCo, reducing $|\mathbf{M}_{\text{Gd}}|$ more than $|\mathbf{M}_{\text{Co}}|$ and therefore reducing T_M . We have shown that the T_M value for GdCo can be shifted by $>100\ \text{K}$, the dominant sublattice can be isothermally switched using pulses as short as $50\ \mu\text{s}$ and devices show no degradation after $>10^4$ gating cycles, making it of potential use for realizing spintronic synapse⁴⁹. The approach allows for voltage-induced net magnetization modulation and switching, and full 180° Néel vector reversal in the absence of an external magnetic field. The localized switching allows for reversed domain and skyrmion generation on racetrack devices, revealing potential applications in solid-state magnetic data storage and logic. We expect that the approach should be applicable to the larger family of RE–TM magnets and be able to control a wide range of properties and phenomena, such as spin dynamics and spin texture characteristics. This localized MOKE contrast switching may have potential applications in an energy-efficient magneto-optical spatial light modulator with high pixel density.

Finally, we note that data from Figs. 1, 3, 4 and 6 and associated text were also presented in ref. ⁵⁰.

Online content

Any methods, additional references, Nature Research reporting summaries, source data, extended data, supplementary information, acknowledgements, peer review information; details of author contributions and competing interests; and statements of data and code availability are available at <https://doi.org/10.1038/s41565-021-00940-1>.

References

1. Fert, A., Cros, V. & Sampaio, J. Skyrmions on the track. *Nat. Nanotechnol.* **8**, 152–156 (2013).
2. Parkin, S. S. P., Hayashi, M. & Thomas, L. Magnetic domain-wall racetrack memory. *Science* **320**, 190–194 (2008).
3. Tsymbal, E. Y. Electric toggling of magnets. *Nat. Mater.* **11**, 12–13 (2011).

4. Liu, L. et al. Spin-torque switching with the giant spin Hall effect of tantalum. *Science* **336**, 555–558 (2012).
5. Heron, J. T. et al. Deterministic switching of ferromagnetism at room temperature using an electric field. *Nature* **516**, 370–373 (2014).
6. Matsukura, F., Tokura, Y. & Ohno, H. Control of magnetism by electric fields. *Nat. Nanotechnol.* **10**, 209–220 (2015).
7. Valencia, S. et al. Interface-induced room-temperature multiferroicity in BaTiO₃. *Nat. Mater.* **10**, 753–758 (2011).
8. Spaldin, N. A. & Ramesh, R. Advances in magnetoelectric multiferroics. *Nat. Mater.* **18**, 203–212 (2019).
9. Baek, S. H. et al. Ferroelastic switching for nanoscale non-volatile magnetoelectric devices. *Nat. Mater.* **9**, 309–314 (2010).
10. Fiebig, M., Lottermoser, T., Meier, D. & Trassin, M. The evolution of multiferroics. *Nat. Rev. Mater.* **1**, 16046 (2016).
11. Cherifi, R. O. et al. Electric-field control of magnetic order above room temperature. *Nat. Mater.* **13**, 345–351 (2014).
12. He, X. et al. Robust isothermal electric control of exchange bias at room temperature. *Nat. Mater.* **9**, 579–585 (2010).
13. Mahmood, A. et al. Voltage controlled Néel vector rotation in zero magnetic field. *Nat. Commun.* **12**, 1674 (2021).
14. Caretta, L. et al. Fast current-driven domain walls and small skyrmions in a compensated ferrimagnet. *Nat. Nanotechnol.* **13**, 1154–1160 (2018).
15. Kim, K. J. et al. Fast domain wall motion in the vicinity of the angular momentum compensation temperature of ferrimagnets. *Nat. Mater.* **16**, 1187–1192 (2017).
16. Cai, K. et al. Ultrafast and energy-efficient spin-orbit torque switching in compensated ferrimagnets. *Nat. Electron.* **3**, 37–42 (2020).
17. Radu, I. et al. Transient ferromagnetic-like state mediating ultrafast reversal of antiferromagnetically coupled spins. *Nature* **472**, 205–209 (2011).
18. Ueda, K., Mann, M., de Brouwer, P. W. P., Bono, D. & Beach, G. S. D. Temperature dependence of spin-orbit torques across the magnetic compensation point in a ferrimagnetic TbCo alloy film. *Phys. Rev. B* **96**, 064410 (2017).
19. Katayama, T., Hasegawa, K., Kawanishi, K. & Tsushima, T. Annealing effects on magnetic properties of amorphous GdCo, GdFe, and GdCoMo films. *J. Appl. Phys.* **49**, 1759–1761 (1978).
20. Ueda, K., Tan, A. J. & Beach, G. S. D. Effect of annealing on magnetic properties in ferrimagnetic GdCo alloy films with bulk perpendicular magnetic anisotropy. *AIP Adv.* **8**, 125204 (2018).
21. Chaudhari, P., Cuomo, J. J. & Gambino, R. J. Amorphous metallic films for magneto-optic applications. *Appl. Phys. Lett.* **22**, 337–339 (1973).
22. Schelleng, J. H., Forester, D. W., Lubitz, P. & Vittoria, C. Hydrogenation and magnetic properties of amorphous rare-earth-iron (R-Fe) alloys. *J. Appl. Phys.* **55**, 1805–1807 (1984).
23. Pourarian, F. Review on the influence of hydrogen on the magnetism of alloys based on rare earth-transition metal systems. *Physica B* **321**, 18–28 (2002).
24. Stanciu, C. D. et al. All-optical magnetic recording with circularly polarized light. *Phys. Rev. Lett.* **99**, 047601 (2007).
25. Kimel, A. V. & Li, M. Writing magnetic memory with ultrashort light pulses. *Nat. Rev. Mater.* **4**, 189–200 (2019).
26. Tan, A. J. et al. Magneto-ionic control of magnetism using a solid-state proton pump. *Nat. Mater.* **18**, 35–41 (2019).
27. Mushnikov, N. V., Goto, T., Gaviko, V. S. & Zajkov, N. K. Magnetic properties of crystalline and amorphous GdCo₂H_x hydrides. *J. Alloys Compd.* **292**, 51–56 (1999).
28. Knapton, A. G. Palladium alloys for hydrogen diffusion membranes. *Platin. Met. Rev.* **21**, 44–50 (1977).
29. Tan, A. J. et al. Hydration of gadolinium oxide (GdO_x) and its effect on voltage-induced Co oxidation in a Pt/Co/GdO_x/Au heterostructure. *Phys. Rev. Mater.* **3**, 064408 (2019).
30. Huang, M. et al. Voltage-gated optics and plasmonics enabled by solid-state proton pumping. *Nat. Commun.* **10**, 5030 (2019).
31. Hansen, P. & Heitmann, H. Media for erasable magneto-optic recording. *IEEE Trans. Magn.* **25**, 4390–4404 (1989).
32. Tsuchida, T., Sugaki, S. & Nakamura, Y. Magnetic properties of GdCo₂ and Gd_{1-x}Y_xCo₂. *J. Phys. Soc. Japan* **39**, 340–343 (1975).
33. Lemaire, R. & Schweizer, J. Variation du moment magnétique du cobalt dans les composés Gd_xY_{1-x}Co₂. *Phys. Lett.* **21**, 366–368 (1966).
34. McGuire, T. R. & Gambino, R. J. Hall effect in amorphous Gd alloy films. *J. Magn. Magn. Mater.* **15–18**, 1401–1403 (1980).
35. Nagaosa, N., Sinova, J., Onoda, S., MacDonald, A. H. & Ong, N. P. Anomalous Hall effect. *Rev. Mod. Phys.* **82**, 1539–1592 (2010).
36. Finley, J. & Liu, L. Spin-orbit-torque efficiency in compensated ferrimagnetic cobalt-terbium alloys. *Phys. Rev. Appl.* **6**, 054001 (2016).
37. Niemier, M. T. et al. Nanomagnet logic: progress toward system-level integration. *J. Phys. Condens. Matter* **23**, 493202 (2011).
38. Breikreutz, S. et al. Controlled reversal of Co/Pt dots for nanomagnetic logic applications. *J. Appl. Phys.* **111**, 07A715 (2012).
39. Haldar, A., Kumar, D. & Adeyeye, A. O. A reconfigurable waveguide for energy-efficient transmission and local manipulation of information in a nanomagnetic device. *Nat. Nanotechnol.* **11**, 437–443 (2016).
40. Choudhury, S. et al. Voltage controlled on-demand magnonic nanochannels. *Sci. Adv.* **6**, eaba5457 (2020).
41. Rapoport, E., Montana, D. & Beach, G. S. D. Integrated capture, transport, and magneto-mechanical resonant sensing of superparamagnetic microbeads using magnetic domain walls. *Lab Chip* **12**, 4433–4440 (2012).
42. Chen, C. et al. Voltage manipulation of magnetic particles using multiferroics. *J. Phys. D* **53**, 174002 (2020).
43. Zhang, D. et al. Enhancement of tunneling magnetoresistance by inserting a diffusion barrier in L1₀-FePd perpendicular magnetic tunnel junctions. *Appl. Phys. Lett.* **112**, 152401 (2018).
44. Zhang, D. et al. L1₀ Fe-Pd synthetic antiferromagnet through an fcc Ru spacer utilized for perpendicular magnetic tunnel junctions. *Phys. Rev. Appl.* **9**, 044028 (2018).
45. Miron, I. M. et al. Perpendicular switching of a single ferromagnetic layer induced by in-plane current injection. *Nature* **476**, 189–193 (2011).
46. Zhao, Z., Smith, A. K., Jamali, M. & Wang, J. External-field-free spin Hall switching of perpendicular magnetic nanopillar with a dipole-coupled composite structure. *Adv. Electron. Mater.* **6**, 1901368 (2020).
47. Streubel, R. et al. Experimental evidence of chiral ferrimagnetism in amorphous GdCo films. *Adv. Mater.* **30**, 1800199 (2018).
48. Emori, S., Bauer, U., Ahn, S.-M., Martinez, E. & Beach, G. S. D. Current-driven dynamics of chiral ferromagnetic domain walls. *Nat. Mater.* **12**, 611–616 (2013).
49. Fukami, S. & Ohno, H. Perspective: spintronic synapse for artificial neural network. *J. Appl. Phys.* **124**, 151904 (2018).
50. Huang, M. *Voltage Control of Electrical, Optical and Magnetic Properties of Materials by Solid State Ionic Transport and Electrochemical Reactions*. PhD thesis, Massachusetts Institute of Technology (2020).

Methods

Sample preparation. All samples were grown using magnetron sputtering. The samples for the MOKE measurements presented in Fig. 1 had a layer structure of Ta (4 nm)/Pd (6 nm)/Gd₄₅Co₅₅ (6 nm)/Pd (10 nm)/GdO_x (30 nm)/Au (3 nm). The samples for XMCD measurements had a layer structure of Ta (4 nm)/Pd (6 nm)/Gd₄₅Co₅₅ (8 nm)/Pd (10 nm)/yttria-stabilized zirconia (YSZ; 30 nm)/Au (3 nm) grown on Si₃N₄ membrane chips with a 500 μm × 500 μm membrane window of thickness 200 nm (Silson). The samples for electrical measurements, reversed domain generation and structural characterization had a layer structure of Ta (3 nm)/Pt (3 nm)/Gd₄₅Co₅₅ (6 nm)/Pd (6 nm)/Al₂O₃ (20 nm)/GdO_x (30 nm)/Au (3 nm). The samples for net magnetization switching and switchable exchange bias studies had a layer structure of NiO (33 nm)/Pd (1 nm)/Gd₄₅Co₅₅ (6 nm)/Pd (10 nm)/GdO_x (30 nm)/Au (3 nm). The samples for the external-field-free switching of sublattices had a layer structure of Cr (15 nm)/Ru (5 nm)/L₁₀-FePd (7.5 nm)/Ta (5 nm)/Al₂O₃ (5 nm)/Ta (4 nm)/Pt (3 nm)/Gd₄₅Co₅₅ (5 nm)/Pd (6 nm)/Gd₂O₃ (20 nm) grown on a (001) single-crystal MgO substrate. All layers were grown at nominal room temperature, except for the growth of Cr (15 nm)/Ru (5 nm)/L₁₀-FePd (7.5 nm) layers, when the substrate temperature was kept at 350 °C. The pressure of the Ar gas was set at 4.5 mtorr for the FePd layer and at 2.0 mtorr for the Cr (15 nm)/Ru (5 nm) layers and the 5-nm Ta layer immediately above the FePd layer. Au was grown under 3.5 mtorr Ar. The rest of the Ta, Pt, Pd and GdCo layers were grown under 3 mtorr Ar sputtering gas. The NiO layer was grown by reactive sputtering under 1.6 mtorr Ar with 0.07 mtorr O₂. The Al₂O₃ layer was grown reactively under 3 mtorr Ar with 0.1 mtorr O₂. The GdO_x and YSZ (8 mol% Y₂O₃) layers were deposited using radiofrequency sputtering with 3 mtorr Ar and 0.7 mtorr O₂. The exchange-biased samples were grown using an out-of-plane bias field of 2.8 kOe. The thickness of the Pd layer between NiO and GdCo was optimized to minimize the reduction of NiO and the oxidation of GdCo while maintaining the exchange bias⁵¹.

Shadow masking was used to pattern the 3-nm top Au electrodes for the MOKE measurements presented in Figs. 1 and 5f, which are of size around 200 × 200 μm. The Hall crosses for achieving field-free sublattice switching had channel dimensions of 400 nm × 400 nm, and were patterned using electron-beam lithography and then ion milling. The other Hall crosses had channel dimensions of 6 μm × 6 μm. The domain wall tracks for reversed domain generation were 200-μm long and 20-μm wide, whereas the tracks for skyrmion generation were 200-μm long and 100-μm wide with a region 80-μm wide and 50-μm long in the centre. These Hall crosses and domain wall tracks were patterned using photolithography followed by ion milling. The Al₂O₃ hydrogen blocking layer, GdO_x electrolyte layer and Au top electrode layer for the Hall crosses and racetracks were patterned using photolithography followed by lift-off. The Al₂O₃ hydrogen blocking layer was only incorporated into the skyrmion racetrack in Fig. 6c and patterned to have a 20-μm diameter circular hole located at the centre of the gate electrode.

Polar laser and wide-field MOKE measurements. MOKE measurements were performed using a 1 mW laser with a wavelength of 660 nm focused to a spot size of about 10 μm, and were performed in polar geometry that is sensitive to out-of-plane magnetization. The sample temperature was controlled by a flow cryostat. Electrical contact with the top Au electrodes was made using a CuBe probe, and electrical contact with the bottom electrode was made through the Pd layer at the sample edge. The hysteresis loops were measured with a laser spot positioned near the centre of the electrodes. The MOKE differential images in Fig. 1c–e were obtained by subtracting the MOKE images obtained after saturating the film along the z– direction from the images obtained after saturating the film along the z+ direction. The MOKE differential images in Fig. 6b,c and Supplementary Fig. 6 were obtained by subtracting the MOKE images obtained before current injection from the MOKE images taken after current injection.

X-ray magnetic circular dichroism. Two identical devices were prepared, and voltage gating was carried out ex situ on one of the two devices prior to X-ray measurements. YSZ was used instead of GdO_x so that the gate oxide did not contribute to the XAS signal of Gd. YSZ has been reported to allow hydrogen gating in solid-state structures similarly to GdO_x with good performance⁵². The XMCD measurements and analysis were performed similarly to previously reported procedures⁵³. The XMCD spectra were measured at the BOREAS beamline of the ALBA synchrotron⁵⁴ with a 90% circularly polarized X-ray beam for the Gd M_{4,5} edge and a 100% circularly polarized X-ray beam for the Co L_{2,3} edge. The X-ray beam was produced by an Apple-II-type undulator. The incident flux signal was normalized using a gold mesh. The measurements were carried out in transmission geometry using a silicon diode at normal incidence in a magnetic field of 1 T parallel to the incoming X-ray. This field strength was chosen to align the net magnetization while avoiding spin flop. For each measurement, two spectra per helicity were recorded. The XMCD configuration allows for extraction of the magnetization along the beam direction as detailed previously^{55,56}. The average XAS spectrum was calculated from the sum of the alternating helicity spectra, whereas the XMCD spectrum was obtained from their difference. The Gd XAS background was corrected by linear interpolation of the off-peak intervals $E < 1,170$ eV, $1,192$ eV $< E < 1,206$ eV and $E > 1,230$ eV, and the Co XAS background

was corrected using the off-peak intervals $E < 775$ eV, 788 eV $< E < 791$ eV and $E > 800$ eV. The magnetizations were calculated by $M_z = -\mu_B/\hbar(L_z + 2S_z)$, where μ_B is the Bohr magneton, \hbar is the reduced Planck constant, L_z is the z-component of the orbital angular momentum, and S_z is the z-component of the spin angular momentum. For Gd, $L_z = 2\hbar n_h q/r$, where $n_h = 7$ is the electron hole number of 4f states for a Gd atom, q is the total XMCD integral of Gd M₄ and M₅ peaks, and r is the total integral over the XAS after background correction. For the calculation of S_z , the formula $S_{\text{eff}} = 2S_z + 6T_z$ was used, where S_{eff} is the effective spin density and T_z is the magnetic dipole term. S_{eff} was calculated by $S_{\text{eff}} = \hbar n_h(5p - 3q)/r$, where p is the XMCD integral of the M₅ peak. Assuming that the ratio of S_z/T_z stays the same as the values for free Gd ions as reported in the literature⁵⁷, which is expressed by $S_z/T_z = S_z^{\text{free}}/T_z^{\text{free}} = -3.466/0.01$, S_z was derived as $S_z = S_{\text{eff}}/(2 + 6T_z^{\text{free}}/S_z^{\text{free}})$. For Co, L_z was calculated as $L_z = 4\hbar n_h q/3r$, where $n_h = 2.5$, q is the total XMCD integral of Co L₂ and L₃ peaks, and r is the total integral over the XAS after background correction. The T_z term was neglected for Co, so S_z was obtained as $S_z = S_{\text{eff}}/2$, and $S_{\text{eff}} = \hbar n_h(6p - 4q)/r$, where $n_h = 2.5$ and p is the XMCD integral of the L₃ peak. For both Gd and Co, the errors of p and q were propagated from the variation of p and q from the actual integration limits.

Mean-field approximation modelling. MFA methods were adapted from ref. 58 and applied to the GdCo system to understand the change in sublattice magnetization as a function of temperature before and after hydrogenation. The molecular fields of the two lattices are given by:

$$\mu_{\text{Gd}} H_{\text{Gd}}^{\text{MFA}} = \mu_{\text{Gd}} H + xzJ_{\text{Gd-Gd}}\sigma_{\text{Gd}} + (1-x)zJ_{\text{Gd-Co}}\sigma_{\text{Co}} \quad (1)$$

$$\mu_{\text{Co}} H_{\text{Co}}^{\text{MFA}} = \mu_{\text{Co}} H + (1-x)zJ_{\text{Co-Co}}\sigma_{\text{Gd}} + xzJ_{\text{Gd-Co}}\sigma_{\text{Gd}} \quad (2)$$

where μ_{Gd} and μ_{Co} are the magnetic moments of Gd and Co, respectively, $H_{\text{Gd}}^{\text{MFA}}$ and $H_{\text{Co}}^{\text{MFA}}$ are the molecular fields acting on the Gd and Co sublattice spins, x is the concentration of Gd ($x = 0.45$ was used in this analysis), σ_{Gd} and σ_{Co} are the spin polarizations of Gd and Co, respectively, H is the external field ($H = 1$ T was used in this analysis), J_{-j} is the exchange coupling strength, and z is the coordination number and was set to 12 for both sublattices. The choice of z does not affect the ratio of the exchange coupling strength before and after gating.

The magnetic moments of Gd and Co were chosen to be the values obtained from the sum rule at low temperature (2 K). The Co magnetic moment is close to the bulk value (1.6–1.7 μ_B)⁵⁶, whereas the Gd magnetic moment is smaller than the bulk value μ_{Gd}^0 (7.63 μ_B)⁵⁹. We assume that this difference primarily arises from the preferential oxidation of Gd during sample fabrication, leading to a non-magnetic GdO_x interfacial layer in the as-grown state. Application of a gate voltage leads to an additional small decrease in the average Gd magnetic moment at low temperature (see Fig. 2b, middle), which we speculate arises from the formation of a non-magnetic hydride phase that coexists with the magnetic hydrogenated GdCo. The ratio of $\mu_{\text{Gd}}/\mu_{\text{Gd}}^0$ is denoted as the magnetic atomic ratio of Gd.

The sublattice magnetization per atom $M_{\text{Co}} = \mu_{\text{Co}}\sigma_{\text{Co}}$ and $M_{\text{Gd}} = \mu_{\text{Gd}}\sigma_{\text{Gd}}$ can be obtained by solving the self-consistent equations:

$$\sigma_{\text{Gd}} = \left(\coth \xi_{\text{Gd}} - \frac{1}{\xi_{\text{Gd}}} \right) \xi_{\text{Gd}} \quad (3)$$

$$\sigma_{\text{Co}} = \left(\coth \xi_{\text{Co}} - \frac{1}{\xi_{\text{Co}}} \right) \xi_{\text{Co}} \quad (4)$$

where

$$\xi_i = \frac{\mu_i H_i^{\text{MFA}}}{k_B T} \quad (5)$$

where μ_i is the magnetic moment of Co or Gd, k_B is the Boltzmann constant and T is the temperature.

The exchange coefficient $J_{\text{Gd-Gd}}$ was neglected in the modelling due to its small amplitude⁶⁰. $J_{\text{Co-Co}}$ and $J_{\text{Gd-Co}}$ were fitted to match the magnetization data from the XMCD sum rules.

The total magnetization per atom can be calculated by:

$$|M_z| = |x\mu_{\text{Gd}}\sigma_{\text{Gd}} + (1-x)\mu_{\text{Co}}\sigma_{\text{Co}}|. \quad (6)$$

Hall effect measurements. AHE measurements were performed using a lock-in amplifier with an alternating voltage source to provide the drive current at a frequency of 10 kHz. The drive current amplitude was 0.6 mA for the 400 nm × 400 nm Hall crosses and 0.3 mA for the 6 μm × 6 μm Hall crosses.

Cycling of dominant sublattice at room temperature. $V_G = +2.3$ V (–0.5 V) was applied at room temperature to switch the device to the Co (Gd)-dominant state. AHE hysteresis loops were acquired every 0.1 s. After each crossing of compensation, the polarity of V_G was switched once a loop with $H_c < 800$ Oe was acquired and met

the criteria of $|M_r|/|M_s| > 0.8$ for at least the last three consecutive loops, where M_r is the remanent magnetization and M_s is the saturation magnetization.

Current pulse injection for racetrack experiments. To move the generated reversed domain along the racetrack, current pulses with a width of 10 μ s were injected through contact pads patterned at either end of the track, and the current density in the Pt layer was 1.1×10^{11} A m⁻². To move the generated bubble skyrmion, current pulses with a width of 200 μ s were injected, and the current density in the Pt layer was 0.8×10^{11} A m⁻². A small, constant out-of-plane field (−10 Oe) was applied after the generation of the reversed bubble skyrmion to maintain its size so that it could remain visible in wide-field MOKE microscopy.

Computational methods. First-principles spin-polarized calculations were performed using DFT and the projector augmented wave method as implemented in the Vienna ab initio simulation package (VASP)⁶⁴. The exchange–correlation potential was treated using the generalized gradient approximation (GGA) with the Perdew–Burke–Ernzerhof functional corrected for solids⁶², with the valence states $5s^2 5p^6 5d^1 6s^2 4f^1$ for Gd and $3d^7 4s^2$ for Co. The GGA+U method⁶⁵ was applied to the Gd f orbitals and the Co d orbitals with effective on-site Coulomb interaction parameter $U_{\text{eff}} = 7$ and 3 eV, respectively. A $7.103 \times 7.103 \times 7.103 \text{ \AA}^3$ supercell of GdCo₂ (C15 Laves phases) was used, which contains 8 Gd and 16 Co atoms. A k -point mesh of $8 \times 8 \times 8$ and an energy cut-off of 400 eV were applied. Our calculations showed that hydrogen solubility is higher for 1Gd3Co tetrahedral pores, so these interstitials were used to simulate hydride formation (see Supplementary Information for more details).

Magnetic coupling constants were calculated from the Heisenberg model of the exchange for nearest neighbours, which is described by the following Hamiltonian:

$$H = -\frac{1}{2} \sum_{ij} J_{i-j} \sigma_i \sigma_j \quad (7)$$

We employed Monte-Carlo simulations as implemented in the VAMPIRE atomistic code⁶⁴ to compute the temperature-dependent equilibrium magnetizations for the GdCo₂H_x, using a supercell of $5.78 \times 5.78 \times 5.78 \text{ nm}^3$ that contains 12,288 Co and Gd atoms. The effect of hydrogen absorption was introduced by modifying the set of exchange correlation constants from the results of ab initio calculations. System trajectories were simulated for various hydrogen concentration under constant $T = 300 \text{ K}$, with 10^7 time steps (after 10^4 equilibration steps) and an integration time step of 10^{-15} s. The zero-field equilibrium magnetizations of the sublattices and the net magnetization were extracted from these trajectories.

All calculations were carried out using XSEDE computational resources⁶⁵.

Data availability

Source data are provided with this paper. The XMCD spectra that support the findings of this study are publicly available at <https://doi.org/10.5281/zenodo.4831735>.

References

1. Gilbert, D. A. et al. Controllable positive exchange bias via redox-driven oxygen migration. *Nat. Commun.* **7**, 11050 (2016).
2. Lee, K.-Y. et al. Fast magneto-ionic switching of interface anisotropy using yttria-stabilized zirconia gate oxide. *Nano Lett.* **20**, 3435–3441 (2020).
3. Caretta, L. et al. Interfacial Dzyaloshinskii-Moriya interaction arising from rare-earth orbital magnetism in insulating magnetic oxides. *Nat. Commun.* **11**, 1090 (2020).
4. Barla, A. et al. Design and performance of BOREAS, the beamline for resonant X-ray absorption and scattering experiments at the ALBA synchrotron light source. *J. Synchrotron Radiat.* **23**, 1507–1517 (2016).
5. Vasilii, H. B. et al. Direct observation of multivalent states and $4f \rightarrow 3d$ charge transfer in Ce-doped yttrium iron garnet thin films. *Phys. Rev. B* **96**, 014433 (2017).
6. Chen, C. T. et al. Experimental confirmation of the X-ray magnetic circular dichroism sum rules for iron and cobalt. *Phys. Rev. Lett.* **75**, 152–155 (1995).
7. Teramura, Y., Tanaka, A., Thole, B. T. & Jo, T. Effect of Coulomb interaction on the X-ray magnetic circular dichroism spin sum rule in rare earths. *J. Phys. Soc. Japan* **65**, 3056–3059 (1996).
8. Ostler, T. A. et al. Crystallographically amorphous ferrimagnetic alloys: comparing a localized atomistic spin model with experiments. *Phys. Rev. B* **84**, 024407 (2011).

9. White, H. W., Beaudry, B. J., Burgardt, P., Legvold, S. & Harmon, B. N. Magnetic moments of ferromagnetic gadolinium alloys. *AIP Conf. Proc.* **29**, 329 (1976).
10. Mansuripur, M. & Ruane, M. Mean-field analysis of amorphous rare earth-transition metal alloys for thermomagnetic recording. *IEEE Trans. Magn.* **22**, 33–43 (1986).
11. Kresse, G. & Furthmüller, J. Efficient iterative schemes for ab initio total-energy calculations using a plane-wave basis set. *Phys. Rev. B* **54**, 11169–11186 (1996).
12. Perdew, J. P. et al. Restoring the density-gradient expansion for exchange in solids and surfaces. *Phys. Rev. Lett.* **100**, 136406 (2008).
13. Dudarev, S. & Botton, G. Electron-energy-loss spectra and the structural stability of nickel oxide: an LSDA+U study. *Phys. Rev. B* **57**, 1505–1509 (1998).
14. Evans, R. F. L. et al. Atomistic spin model simulations of magnetic nanomaterials. *J. Phys. Condens. Matter* **26**, 103202 (2014).
15. Towns, J. et al. XSEDE: accelerating scientific discovery. *Comput. Sci. Eng.* **16**, 62–74 (2014).

Acknowledgements

This work was supported in part by the US National Science Foundation (NSF) through the Massachusetts Institute of Technology Materials Research Science and Engineering Center (MRSEC) under award number DMR-1419807 and through NSF award number ECCS-1808828, by SMART, one of seven centres of nCORE, a Semiconductor Research Corporation program, sponsored by the National Institute of Standards and Technology (NIST), by DARPA ERI FRANC program under HR001117S0056-FP-042, by the DARPA TEE program under HR001117S0038-D18AC0019, by the Korea Institute of Science and Technology (KIST) Institutional Program (2E31032) and a National Research Council of Science and Technology (NST) grant (CAP-16-01-KIST) by the Korea government (MSIP), and by the German Science Foundation (DFG) under project 400178764. This work used the Extreme Science and Engineering Discovery Environment (XSEDE) computational resources provided through allocation TG-DMR190038. The work was performed using the facilities in the MIT Microsystems Technology Laboratory and in the Center for Materials Science and Engineering, supported by the NSF MRSEC program under award number DMR-1419807. Portions of this work were conducted in the Minnesota Nano Center, which is supported by the NSF through the National Nanotechnology Coordinated Infrastructure (NNCI) under award number ECCS-2025124. M.V. and P.G. acknowledge additional funding through grants from MINECO FIS2016-78591-C3-2-R (AEI/FEDER, UE) and FLAG-ERA SographMEM (PCI2019-111908-2). M.H. acknowledges financial support from the Kavanaugh Fellows Program in the Department of Materials Science and Engineering at MIT. L.C. acknowledges financial support from the NSF Graduate Research Fellowship and the GEM Consortium. The authors thank L. Liu for use of ion-milling equipment.

Author contributions

M.H. and G.S.D.B. conceived and designed the experiments. G.S.D.B., J.C., K.L., B.Y. and J.-P.W. supervised the respective members of the study. M.H., M.U.H., D.Z., D.L. and J.Z. fabricated the samples. M.H., M.U.H. and J.Z. performed MOKE and electrical characterizations. S.S., A.C., P.G., M.V. and M.H. conducted the XMCD measurements. M.H. and E.B. processed the XMCD measurements with help from M.V. and P.G. M.H. carried out the mean-field modelling. K.K. performed the ab initio and spin dynamics calculations. M.H. set up the temperature-dependent MOKE apparatus with help from L.C. K.-Y.L. performed the structural and chemical analyses. M.H. wrote the manuscript with guidance from G.S.D.B. All authors discussed the results and commented on the manuscript.

Competing interests

The authors declare no competing interests.

Additional information

Supplementary information The online version contains supplementary material available at <https://doi.org/10.1038/s41565-021-00940-1>.

Correspondence and requests for materials should be addressed to G.S.D.B.